Dynamical Piezomagnetic Effect in Time-Reversal-Invariant Weyl Semimetals with Axionic Charge-Density Waves

Jiabin Yu
University of Maryland
Benjamin Wieder
Massachusetts Institute of Technology https://orcid.org/0000-0003-2540-6202
Chao-xing Liu (lcxlight@gmail.com)
The Pennsylvania State University

Article

Keywords: dynamical piezomagnetic effect, orbital magnetization

Posted Date: June 10th, 2021

DOI: https://doi.org/10.21203/rs.3.rs-577649/v1

Dynamical Piezomagnetic Effect in Time-Reversal-Invariant Weyl Semimetals with Axionic Charge-Density Waves

Jiabin Yu,[1,2] Benjamin J. Wieder,[3,4,5] and Chao-Xing Liu[1,*]

[1] *Department of Physics, the Pennsylvania State University, University Park, PA 16802*
[2] *Condensed Matter Theory Center, Department of Physics, University of Maryland, College Park, Maryland 20742, USA*
[3] *Department of Physics, Massachusetts Institute of Technology, Cambridge, MA 02139, USA*
[4] *Department of Physics, Northeastern University, Boston, MA 02115, USA*
[5] *Department of Physics, Princeton University, Princeton, New Jersey 08544, USA*

We predict that dynamical strain can induce a bulk orbital magnetization in time-reversal- (TR-) invariant Weyl semimetals (WSMs) that are gapped by charge-density waves (CDWs) – a class of systems experimentally observed this past year. We term this effect the "dynamical piezomagnetic effect" (DPME). By studying the low-energy effective theory and a minimal tight-binding (TB) model, we find that the DPME originates from an effective valley axion field that couples the electromagnetic gauge field with a strain-induced pseudo-gauge field. In particular, the DPME represents the first example of a fundamentally 3D strain effect originating from the Chern-Simons 3-form, in contrast to the previously-studied piezoelectric effects characterized by 2D Berry curvature. We further find that the DPME has a discontinuous change when the surface of the system undergoes a topological quantum phase transition (TQPT), and thus, that the DPME provides a bulk signature of a boundary TQPT in a TR-invariant Weyl-CDW.

CONTENTS

I. INTRODUCTION

The last four decades have witnessed a paradigm shift in condensed matter physics driven by the discovery of the geometric phase and topology of electronic wave functions[1,2]. The search for experimentally observable response signatures of bulk nontrivial topology has emerged as central to the advancement of solid-state physics and material science. In two-dimensional (2D) systems, the Berry curvature in momentum space not only provides an essential contribution towards quantized topological response effects, such as the quantum Hall effect and the quantum anomalous Hall effect (QAHE)[3–6], but also provides non-negligible contributions to various non-quantized physical phenomena, such as the intrinsic anomalous Hall effect[7], orbital magnetic moments[8–10], and the nonlinear Hall effect[11–15]. More recently, it has been demonstrated that the piezoelectric response can also be related to the Berry curvature[16–20], and can have a discontinuous change across a topological quantum phase transition (TQPT) in 2D TR-invariant systems[21]. A natural question to ask is whether a strain-induced response can be related to the topological property of three-dimensional (3D) systems beyond the Berry curvature contribution.

In this work, we answer this question in the affirmative by demonstrating, for the first time, the existence of a *fundamentally 3D* topological strain effect, which we term the "dynamical piezomagnetic effect" (DPME). To begin, let us first focus on a 3D topological electromagnetic response governed by effective axion electrodynamics[22,23]

$$S_{eff,\theta} = \frac{e^2}{32\pi^2}\int dt d^3r \theta \varepsilon^{\mu\nu\rho\delta} F_{\mu\nu}F_{\rho\delta}\ , \qquad (1)$$

where (and for the remainder of this work unless otherwise specified) we choose units in which $\hbar = c = 1$, and notation in which duplicated indices are summed over for notational simplicity. In Eq. (1), $F_{\mu\nu} = \partial_\mu A_\nu - \partial_\nu A_\mu$ is the field strength of the electromagnetic $U(1)$ gauge field A_μ, and θ is the effective axion field. The bulk average value of θ in a 3D gapped crystal with vanishing Hall conductivity, labeled as θ^{bulk}, is determined by the Chern-Simons 3-form[22] instead of the 2D Berry curvature, and θ^{bulk} is only well defined modulo 2π. The winding of θ^{bulk} incorporating a fourth dimension, such as a periodic pumping (Floquet) parameter, gives the second Chern number[22]. As θ^{bulk} has the same transformation properties as $\boldsymbol{E}\cdot\boldsymbol{B}$, any symmetry that flips the sign of $\boldsymbol{E}\cdot\boldsymbol{B}$ (*i.e.*, "axion-odd" symmetries) can quantize θ^{bulk} to 0 or π modulo 2π, providing a symmetry-

protected $\mathbb{Z}_2$ indicator of axionic bulk topology in 3D insulators[22–36]. A direct physical consequence of nonzero θ^{bulk} is the magnetoelectric effect[22], where an external electric (magnetic) field induces a magnetization (polarization) in the parallel direction; if quantized by an axion-odd symmetry, the effect is called the topological magnetoelectric effect[22,37,38]. Other physical consequences of a non-zero θ^{bulk} include the surface half QAHE[22], a giant magnetic-resonance-induced current[39–41], the topological magneto-optical effect[42–44] (especially its exact quantization[42]), the zero-Hall plateau state[45–47], and the image magnetic monopole[48].

In this work, we explore the role of a "valley-separated" variant of an effective axion field in the physical response induced by dynamical strain. In particular, we propose that dynamical homogeneous strain can induce a nonzero bulk-uniform magnetization in a class of 3D TR-invariant insulators that have vanishing total θ^{bulk} (thus a vanishing magnetoelectric response) but have a non-quantized and tunable θ per valley. We term the strain-induced magnetoelectric response the DPME. To be more specific, for the DPME to be relevant to experimental probes, we require a 3D TR-invariant insulator to have (i) low-energy physics that is well captured by a pair of TR-related valleys in the first Brillouin zone, and (ii) non-vanishing valley axion fields, despite exhibiting an overall trivial θ^{bulk}.

Inspired by Ref. [49–51], we recognize that the above requirements for observing the DPME are satisfied by a TR-invariant WSM with a bulk-constant CDW. We emphasize that in this work, the CDW order parameter is taken to be constant (*i.e.* static and homogeneous) in the bulk of the system, in contrast to Ref. [49–51], which focused on bulk fluctuations of the CDW order parameter. By studying the low-energy effective theory of a TR-invariant Weyl-CDW, we find that the phase of the CDW order parameter determines the valley axion field, leading to effective *valley* axion electrodynamics. Combined with the fact that dynamical strain can act as a pseudo-gauge field in WSMs[52–63], we find that the strain-induced pseudo-gauge fields can couple to the electromagnetic field and the valley axion field, resulting in a strain-induced analogue of valley axion electrodynamics: the DPME. The results derived from the low-energy effective theory are further verified against the UV completion by performing a TB calculation. Interestingly, both low-energy effetive theory and our TB calculation suggest that a discontinuous change in the DPME can be driven by a surface $\mathbb{Z}_2$ TQPT without closing the bulk gap. Hence, our findings suggest that jumps in the DPME can serve as bulk signatures of boundary TQPTs.

Crucially, the bulk response coefficient of the DPME is the average value of valley axion field that is determined by the Chern-Simons 3-form. As the Chern-Simons 3-form can only exist in three or higher dimensions, the DPME has a completely different origin compared to previously studied piezoelectric effects, which instead originate from the 2D Berry curvature[16–21]. As a result,

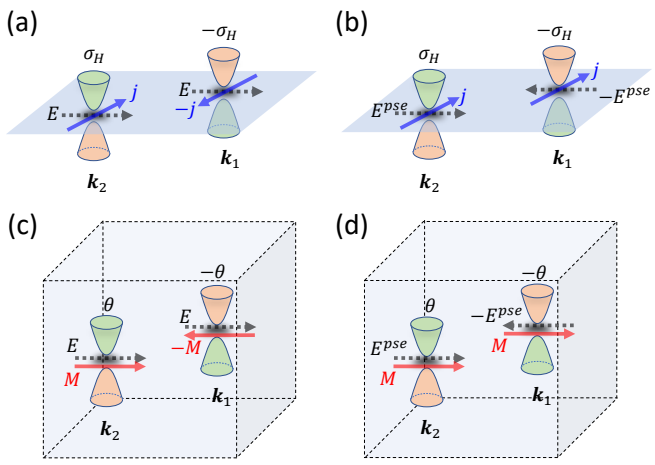

FIG. 1. **2D and 3D response effects in insulators with two valleys.** In (a) and (b), two 2D gapped Dirac cones at $\boldsymbol{k}_{1,2}$ are related by TR symmetry. The two massive 2D Dirac cones provide opposite and canceling contributions to the Hall conductance σ_H. In (c) and (d), two 3D gapped Dirac cones at $\boldsymbol{k}_{1,2}$ are related by TR symmetry. The two 3D Dirac cones have complex masses and have opposite axion fields θ, due to TR symmetry.

the DPME cannot be realized by trivially stacking of 2D systems with nontrivial piezoelectric effects. In this sense, the generalization from 2D piezoelectricity to the 3D DPME is analogous to that from the 2D quantum spin-Hall insulator to the 3D TR-invariant strong topological insulator (TI). Specifically, the 3D TR-invariant strong TI cannot be constructed from a simple 3D stacking of 2D quantum spin-Hall insulators, which instead gives a *weak* TI (WTI). Conversely, the TR-invariant strong TI – a fundamentally 3D phase of matter – was discovered through more involved theoretical efforts[1,2]. Hence, the DPME *cannot* be viewed as a simple 3D generalization of 2D piezoelectricity – the DPME is instead an intrinsically 3D effect.

II. RESULTS

In this section, we will first present an intuitive picture for the DPME. We will then present the low-energy effective theory and a supporting TB calculation demonstrating the existence of the DPME. Lastly, we will describe the discontinuous change of DPME that occurs due to a boundary TQPT.

A. Intuitive Picture

Before presenting supporting analytic and numerical calculations, we will first provide an intuitive picture of the DPME, in comparison with the Berry-curvature contribution to the piezoelectric response[16–21]. We s-

tart with a 2D TR-invariant insulator whose low-energy physics is described by two 2D gapped Dirac cones (regarded as two valleys below), as shown in Fig. 1(a). Because two valleys are related by TR symmetry, there must be an oppositely-signed valley Hall conductance within each valley (determined by the integral of the Berry curvature over each valley), and the Hall currents induced by a uniform electric field must point in opposite directions and exactly cancel. However, a non-vanishing charge current can still be generated by applying a *pseudo*-electric field that points in opposite direction in each valley, which causes the induced Hall currents to point in the same directions and add up to a nonzero total current (Fig. 1(b)). The pseudo-electric field can be generated by a dynamical homogeneous strain tensor u as $E^{pse} \sim \dot{u}$[54,62], and the resultant total Hall current $j \sim \dot{u}$ characterizes the piezoelectric effect[16–20]. With regards to TR symmetry, a static external electric field preserves TR symmetry whereas a static external pseudo-electric field breaks TR symmetry, explaining the dramatic differences in the current response. Although the piezoelectric effect is not quantized in one insulating phase, its nonzero discontinuous *change* across a 2D TR-invariant TQPT (*e.g.* a 2D $\mathbb{Z}_2$ TQPT[64]) is proportional to the change of a topological invariant[21] and thus serves as a new experimental probe of the topology (or more precisely a change in topology).

Although the strain also acts as a pseudo-electric field in the 3D DPME, the 3D DPME is fundamentally distinct from a trivial stacking of the 2D piezoelectric effect, as the 3D DPME originates from the 3D axion field instead of the Hall conductance. To see this, consider a TR-invariant 3D gapped system whose low-energy physics is captured by two 3D gapped Dirac cones with complex masses (also regarded as two valleys below), as shown in Fig. 1(c) and (d). Because the TR symmetry maps one valley to the other, a single Dirac cone is not necessarily TR-invariant, and, in the absence of additional crystal symmetries, generically has an unpinned effective axion field θ. For a finite-sized configuration of the 3D system with a fully gapped TR-invariant 2D boundary, TR symmetry requires that the two Dirac cones have opposite θ angles, implying that an external electric field would induce opposite magnetizations in the two valleys (Fig. 1(c)), which sum to zero. In contrast, a pseudo-electric field, which can be induced by dynamical homogeneous strain and points in opposite directions at each valley, would induce the same magnetizations at the two valleys (Fig. 1(d)), resulting in a nonzero total magnetization $M \propto E^{pse} \sim \dot{u}$. We term this effect the DPME. The DPME is different from the conventional piezomagnetic effect[65] because the magnetization of the former is proportional to the time derivative of the strain tensor $\dot{u}$, whereas the magnetization of the latter is directly proportional to the strain tensor u. Crucially, the bulk average value of the effective axion field θ is determined by the integrals of the Chern-Simons 3-form[22–24] $\epsilon^{ijl}\,\mathrm{Tr}[\mathcal{A}_i\partial_{k_j}\mathcal{A}_l + \mathrm{i}\frac{2}{3}\mathcal{A}_i\mathcal{A}_j\mathcal{A}_l]d^3k$, where $\mathcal{A}$ is the non-Abelian Berry connection, and the Chern-Simons 3-form can only exist in three or higher dimensions. Therefore, unlike the 2D piezoelectric effects, the θ-induced 3D DPME originates from the Chern-Simons 3-form instead of the Berry curvature, meaning that the DPME is intrinsically 3D and cannot be given by trivial stacking systems with a 2D piezoelectric effect.

B. Low-Energy Effective Theory for the DPME

In this section, we will provide a low-energy theory for the DPME in TR-invariant WSMs with axionic CDWs. We emphasize that the derivation below is not confined to Weyl-CDWs, and can be generalized to any TR-invariant system with valley axion fields.

A TR-invariant WSM phase can only emerge in systems that break inversion symmetry (non-centrosymmetric crystals). Fig. 2(a) schematically shows a distribution of four Weyl points in a minimal TR-invariant WSM. The momenta of the four Weyl points take the form

$$\boldsymbol{k}_{a,\alpha} = (-1)^{a-1}(\alpha k_{0,x}, k_{0,y}, \alpha k_{0,z}) \ , \tag{2}$$

where $\alpha = \pm$ indicates the relative chirality of the Weyl points, and $a = 1, 2$ is termed the "valley index." Here we have enforced an additional mirror symmetry that flips y, labeled as m_y, to make the four Weyl points completely symmetry-related, but mirror symmetry is not essential for the physics discussed below.

The low-energy Lagrangian of the four Weyl points can always be transformed into the following form[49]

$$\mathcal{L}_{a,\alpha} = \psi^\dagger_{t,\boldsymbol{r},a,\alpha}\left[\mathrm{i}\partial_t - \alpha\sum_i v_i(-\mathrm{i}\partial_i - k_{a,\alpha,i})\sigma_i\right]\psi_{t,\boldsymbol{r},a,\alpha} \ , \tag{3}$$

where $\psi_{t,\boldsymbol{r},a,\alpha}$ is a two-component field for the two bands that form the Weyl point at $\boldsymbol{k}_{a,\alpha}$, $\sigma_{0,x,y,z}$ are the Pauli matrices, v_i indicates the Fermi velocity along the i direction, and t and $\boldsymbol{r}$ are time and position, respectively. In this work, we will for simplicity focus on the case in which $i = x, y, z$ are the three laboratory directions. Throughout this part on the low-energy theory, we adopt a proper rescaling of the space and fields to cancel the Fermi velocities as discussed in Appendix A and F of the Supplementary Materials (SM); the Fermi velocities will later be restored for comparison to the TB model.

We further introduce a symmetry-preserving static mean-field CDW term[49] $m(\boldsymbol{r})$ that couples two Weyl points of the same valley index, where the CDW wavevector is $\boldsymbol{Q} = \boldsymbol{k}_{1,+} - \boldsymbol{k}_{1,-} = -(\boldsymbol{k}_{2,+} - \boldsymbol{k}_{2,-})$ as shown in Fig. 2(a). In general, $m(\boldsymbol{r}) = |m(\boldsymbol{r})|e^{\mathrm{i}\phi(\boldsymbol{r})}$ is complex, and $|m(\boldsymbol{r})|$ and $\phi(\boldsymbol{r})$ are the magnitude and phase of the CDW order parameter, respectively. We consider m to be constant in the bulk, *i.e.*, $|m(\boldsymbol{r})| = |m_0|$ and $\phi(\boldsymbol{r}) = \phi_0$ for $\boldsymbol{r}$ in the bulk, and we set $|m(\boldsymbol{r})| \to \infty$ and $\phi(\boldsymbol{r}) = 0$ for $\boldsymbol{r}$ deep in the vacuum[22]. We also introduce

an electron-strain coupling for normal strain (*i.e.* stretch or compression along a specified axis) along the z direction, labeled as $u_{zz}(t)$, which is adiabatic, homogeneous, and infinitesimal. Then, combined with the $U(1)$ gauge field coupling for the electromagnetic field, we arrive at the total low-energy Lagrangian $\mathcal{L} = \sum_a \mathcal{L}_a$ with

$$\mathcal{L}_a = \overline{\psi}_a \left[\mathrm{i}(\partial\!\!\!/ + \mathrm{i}e\widetilde{A\!\!\!/}_a - \mathrm{i}\partial\!\!\!/\varphi_a - \mathrm{i}A\!\!\!/_{a,5}\gamma^5) - |m|e^{-\mathrm{i}\Phi_a\gamma^5} \right] \psi_a \ , \tag{4}$$

where $\overline{\psi}_a = \psi_a^\dagger\gamma^0$, $\varphi_a = (\boldsymbol{k}_{a,+} + \boldsymbol{k}_{a,-}) \cdot \boldsymbol{r}/2$, $\Phi_a(\boldsymbol{r}) = (-1)^{a-1}(\phi(\boldsymbol{r}) + \boldsymbol{Q} \cdot \boldsymbol{r})$, and the metric is chosen as $(-,+,+,+)$. Further details are provided in the Methods section.

$\mathcal{L}_a$ describes a massive 3D Dirac fermion that couples to a valley-dependent $U(1)$ gauge field $\widetilde{A}_a$ and a valley-dependent chiral gauge field $A_{a,5}$, and Φ_a is the mass phase of the Dirac fermion. In terms of u_{zz} and the CDW wavevector $\boldsymbol{Q}$, the valley-dependent chiral gauge field is given by

$$A_{a,5,\mu} = (-1)^{a-1}\partial_\mu(\boldsymbol{Q} \cdot \boldsymbol{r}/2) + (-1)^a u_{zz}(0, \xi_x, 0, \xi_z)_\mu \ . \tag{5}$$

Here $\xi_{0,x,y,z}$ are the material-dependent electron-strain couplings. The valley-dependent $U(1)$ gauge field takes the form

$$\widetilde{A}_{a,\mu} = A_\mu + \frac{u_{zz}}{e}(\xi_0, 0, (-1)^{a-1}\xi_y, 0)_\mu \ , \tag{6}$$

which contains the physical gauge field A_μ and the pseudo-gauge field induced by the strain u_{zz}. In particular, the y component of the pseudo-gauge field can provide a pseudo-electric field that points in opposite directions in each of the two valleys

$$\boldsymbol{E}_a^{pse} = (-1)^a \frac{\xi_y}{e} \dot{u}_{zz} \boldsymbol{e}_y \ . \tag{7}$$

As we will show below, all the nontrivial leading-order linear response comes from the pseudo-electric field in Eq. (7).

The low-energy response to A and u_{zz} can be derived from the total effective action $S_{eff} = \sum_a S_{eff,a}$, which takes the form

$$e^{\mathrm{i}S_{eff,a}} = \int D\overline{\psi}_a D\psi_a \exp\left[\mathrm{i}\int dt d^3r \mathcal{L}_a\right] \ . \tag{8}$$

Owing to the valley $U(1)$ gauge invariance and the effective Lorentz invariance, Fujikawa's method suggests that the effective action would contain a topologically nontrivial term[66,67] as

$$S_{eff,a} = \int dt d^3r \frac{e^2}{16\pi^2}\frac{\Phi_a}{2}\varepsilon^{\mu\nu\rho\delta}\widetilde{F}_{a,\mu\nu}\widetilde{F}_{a,\rho\delta} + \dots \ , \tag{9}$$

where $\widetilde{F}_{a,\mu\nu} = \partial_\mu\widetilde{A}_{a,\nu} - \partial_\nu\widetilde{A}_{a,\mu}$, and "..." includes all other terms. In this work, we only consider the leading-order linear response to A and u_{zz}. Through an explicit evaluation of Feynman diagrams in Appendix A and F of the SM, we find that the only leading-order linear response contained in "..." is the trivial correction to the permittivity and permeability in the material, which can be absorbed into the Maxwell term of A. Hence, all nontrivial leading-order linear responses come from the first term of Eq. (9).

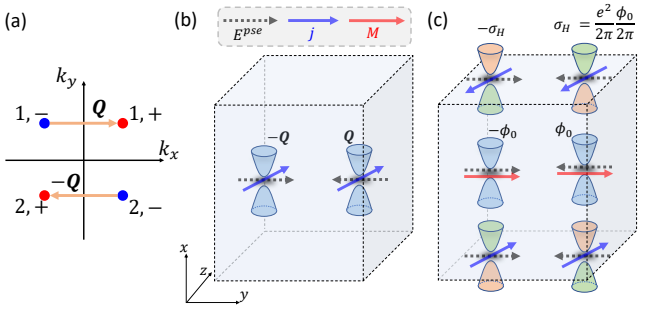

FIG. 2. **Schematic for the DPME induced by the pseudo-electric field in a TR-invariant minimal WSM with a CDW.** (a) The projection of four Weyl points on the $k_x - k_y$ plane in a TR-invariant minimal WSM. The arrows in (a) indicate the projection of the CDW wavevectors $\boldsymbol{Q}$. (b) The low-energy piezoelectric current induced by the CDW wavevector. The dashed box above (b) indicates that the black dashed arrows, the blue solid arrows, and the red solid arrows in (b) and (c) respectively represent the pseudo-electric field, current, and magnetization. (c) The DPME induced by the phase of the CDW order parameter. In (c), we have chosen open boundary conditions for only the surfaces perpendicular to x; the two x-normal surfaces are gapped and symmetry-preserving. The two bulk Dirac cones have opposite bulk phases of the CDW order parameter. Through the bulk-boundary correspondence, this implies that the two valleys have opposite surface Hall conductances.

After omitting all of the higher-order and trivial terms, we arrive at the total effective action as

$$S_{eff} = \int dt d^3r \sum_a \boldsymbol{A} \cdot \left[(-\frac{e^2}{4\pi^2}\nabla\theta_a + \boldsymbol{\Sigma}_{H,a}) \times \boldsymbol{E}_a^{pse} \right] \ , \tag{10}$$

where θ_a is the valley axion field given by the phase of the CDW order parameter as

$$\theta_a = (-1)^{a-1}\phi \ , \tag{11}$$

and $\boldsymbol{\Sigma}_{H,a}$ is the valley Hall conductivity given by the CDW wavevector $\boldsymbol{Q}$

$$\boldsymbol{\Sigma}_{H,a} = (-1)^a \frac{\boldsymbol{Q}}{2\pi}\frac{e^2}{2\pi} \ . \tag{12}$$

TR symmetry enforces that the valley axion field and the valley Hall conductivity have opposite signs in each of the two valleys, resulting in a vanishing electromagnetic response.

The total current derived from S_{eff} can be decomposed into two parts

$$\boldsymbol{j} = \frac{\delta S_{eff}}{\delta \boldsymbol{A}} = \boldsymbol{j}_{PE} + \boldsymbol{j}_M \ . \tag{13}$$

$\boldsymbol{j}_{PE}$ is the total low-energy valley Hall current induced by the pseudo-electric field

$$\boldsymbol{j}_{PE} = \sum_a \boldsymbol{\Sigma}_{H,a} \times \boldsymbol{E}_a^{pse}, \tag{14}$$

which, as required by m_y symmetry, lies in the xz plane, and is schematically shown in Fig. 2(b). According to Eq. (7) and Eq. (12), $\boldsymbol{j}_{PE}$ is actually the bulk-uniform piezoelectric current induced by the CDW wavevector $\boldsymbol{Q}$, where the piezoelectric coefficient is given by

$$\chi_{izz} = \frac{\partial j_{PE,i}}{\partial \dot{u}_{zz}} = \frac{e}{2\pi^2}\xi_y \left(\boldsymbol{Q} \times \boldsymbol{e}_y\right)_i \ . \tag{15}$$

Hence, $\boldsymbol{j}_{PE}$ can be understood as a 3D stack of 2D valley Hall systems in which each layer exhibits the 2D piezoelectric effect discussed in previous literature[18–21].

In Eq. (13), $\boldsymbol{j}_M$ takes the form of a magnetization current

$$\boldsymbol{j}_M = \nabla \times \boldsymbol{M} \tag{16}$$

in which the total orbital magnetization $\boldsymbol{M}$ is induced by a pseudo-electric field through the valley axion field

$$\boldsymbol{M} = -\sum_a \frac{e^2}{4\pi^2}\theta_a \boldsymbol{E}_a^{pse} \ . \tag{17}$$

Physically, Eq. (16) can be understood from the bulk-boundary correspondence as follows. First, given a gapped and symmetry-preserving boundary, the CDW phase ϕ smoothly changes from a constant value ϕ_0 in the bulk to zero in the vacuum, implying that the magnetization current $\boldsymbol{j}_M$ is localized on the boundary. According to the bulk-boundary correspondence of the axion field, the surface valley Hall conductance (along the normal direction of the surface) should take the form $\sigma_{H,a} = \frac{e^2}{2\pi}\frac{\theta_a^{bulk}}{2\pi}$ on any surface, where $\theta_a^{bulk} = (-1)^{a-1}\phi_0$. Hence, the surface-localized magnetization current $\boldsymbol{j}_M$ is simply the surface Hall current induced by the pseudo-electric field, as shown in Fig. 2(c). The surface current generates a uniform bulk magnetization of the form

$$\boldsymbol{M}^{bulk} = -\sum_a \frac{e^2}{2\pi}\frac{\theta_a^{bulk}}{2\pi}\boldsymbol{E}_a^{pse} = \frac{e\xi_y}{2\pi^2}\phi_0 \dot{u}_{zz}\boldsymbol{e}_y \ , \tag{18}$$

which is the DPME proposed in this work, as illustrated in Fig. 1(d). Unlike the piezoelectric current in Eq. (14) originating from the 2D valley Hall conductance, $\boldsymbol{j}_M$ in Eq. (16) originates from the *fundamentally 3D* bulk valley axion field, and is hence fundamentally different from Eq. (14).

C. TB Realization of the DPME

The above analysis is based on low-energy effective field theory. It is natural to ask whether our low-energy prediction of a DPME in TR-invariant Weyl-CDWs remains valid in the presence of high-energy bands (or equivalently in a UV completion). To address this question, we will construct a minimal TB model of a TR-invariant Weyl-CDW and compute the DPME, which we will compare to that predicted by the effective action.

Prior to the onset of a CDW, we begin with an orthorhombic lattice, in which we choose for simplicity the lattice constants to be $a_x = a_y = a_z = a_0$. We then consider there to be two sublattices in each unit cell. We next place a Kramers pair of spinful s orbitals on one sublattice and a Kramers pair of spinful p_y orbitals on the other sublattice. We then construct a four-band TB model (at this stage without a CDW) that preserves TR and m_y symmetries. The explicit form of the TB model is provided in the Methods section. With the parameter values specified in the Methods section, we realize a state with four Weyl points located at

$$\boldsymbol{k}_{a,\alpha} = (-1)^{a-1}(\alpha\frac{\pi}{2a_0}, \frac{\pi}{4a_0}, 0) \ , \tag{19}$$

where the Weyl points are related by TR and m_y symmetries.

We next add a CDW term that preserves TR and m_y symmetries into the TB model. Unlike Ref. [68], we do not study the microscopic origin of the CDW order parameter in this work, as the main goal of introducing the TB model is simply to provide a UV completion of the low-energy theory on which our analysis is rigorously based. In particular, the CDW that we introduce is commensurate to the original lattice, resulting in reduced lattice translation symmetries with the new lattice constants given by $a_x' = 2a_0$, $a_y' = a_0$, and $a_z' = a_0$. The CDW backfolds two Weyl points of the same valley index onto the same momentum in the reduced first Brillouin zone

$$\boldsymbol{k}_a' = (-1)^{a-1}(\frac{\pi}{a_x'}, \frac{\pi}{4a_y'}, 0) \tag{20}$$

to form an unstable 3D Dirac fermion, which then becomes gapped. The explicit expression for the TB model of the Weyl-CDW state and its relation to the low-energy effective action are provided in the Methods section.

Now we use the full TB model to verify the strain-induced piezoelectric effect and the DPME described by Eq. (10). We consider a slab configuration with N layers perpendicular to x with periodic boundary conditions along y and z. Then, we calculate the 2D z-directional strain-induced current density of each layer for $N = 20$ and for various values of ϕ_0 (See Appendix G.4 for details). We note that the current along the y direction conversely vanishes in our numerics at each value of ϕ_0, due to the bulk m_y symmetry.

In Fig. 3(a), we plot the current density distribution $j_z^{2D}(l_x')$ for $\phi_0 = -0.9\pi, -0.45\pi, 0, 0.45\pi, -0.9\pi$, where $l_x' = 1, 2, ..., N$ is the layer index. As schematically shown in Fig. 3(b), we can decompose the current density distribution into a uniform background current $\langle j_z^{2D}\rangle$ (averaged over the layer index) and a layer-dependent part

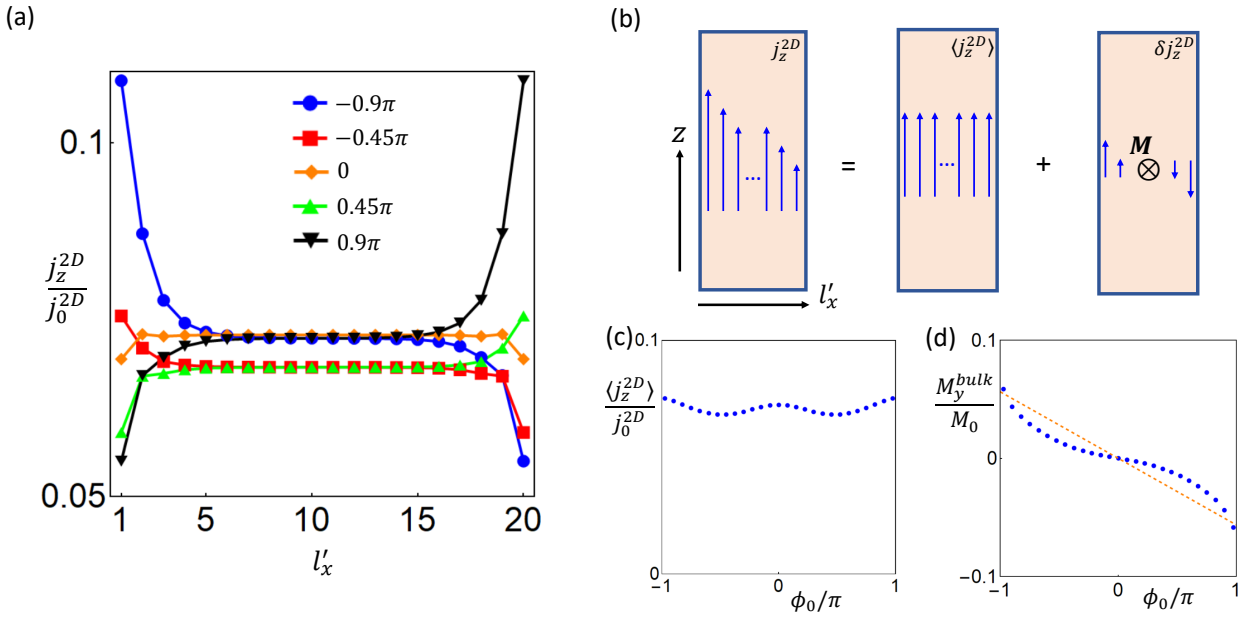

FIG. 3. **TB calculation for the piezoelectric effect and DPME in a TR-invariant WSM with a CDW.** (a) The layer distribution of the 2D strain-induced z-directed current density in the slab configuration of the TB model for several typical values of ϕ_0. (b) The current distribution can be split into a uniform background current and the nonuniform magnetization current. (c) The spatial average of the 2D current density as a function of ϕ_0, where $j_0^{2D} = e\dot{u}_{zz}/a_0$. (d) The ϕ_0 dependence of the bulk magnetization along y, where the blue dots and orange dashed line indicate data obtained from the TB model and the effective action (Eq. (10)), respectively.

$\delta j_z^{2D}(l'_x) = j_z^{2D}(l'_x) - \langle j_z^{2D}\rangle$. The uniform background current $\langle j_z^{2D}\rangle$ characterizes the uniform piezoelectric response, and, as shown in Fig. 3(c), the piezoelectric current is nearly independent of ϕ_0, as expected from the low-energy expression Eq. (16). We would like to emphasize that it is meaningless to compare the exact value predicted by the low-energy Eq. (15) to the TB results in Fig. 3(c), since Eq. (15) only includes the low-energy contribution to the piezoelectric current, while the high-energy contribution to the piezoelectric current is large in the TB model.

On the other hand, the layer-dependent contribution to the layer current density $\delta j_z^{2D}(l'_x)$ is asymmetrically distributed. Specifically, $\delta j_z^{2D}(l'_x)$ exhibits opposite signs near the two surfaces, resulting in a bulk magnetization M_y^{bulk}. We plot the M_y^{bulk} calculated from the TB model as a function of ϕ_0 in Fig. 3(d). To compare with the TB result, we restore the Fermi velocity for the low-energy expression Eq. (18) and substitute in the parameter values shown in Methods, from which we obtain

$$\frac{\boldsymbol{M}_{bulk}}{M_0} = \frac{a_0\xi_y \mathrm{sgn}(v_x v_y v_z)}{2\pi^2 v_y}\phi_0 \boldsymbol{e}_y = -\frac{1}{4\pi^2\sqrt{2}}\phi_0 \boldsymbol{e}_y \ , \quad (21)$$

where $M_0 = e\dot{u}_{zz}/a_0$. As shown in Fig. 3(d), the TB and low-energy results are of the same order of magnitude (the deviation is smaller than 70% of the low-energy result). This coincides with the fact that the valley axion field of the TB model mainly comes from the low-energy modes, as discussed in Appendix B and G of the SM. In particular, the TB and low-energy results in Fig. 3(c) match extremely well as ϕ_0 approaches $\pm\pi$ (the deviation is smaller than 7% of the low-energy result). As discussed below, the agreement between the TB and low-energy results can be attributed to the TB model exhibiting boundary gap closings at exactly $\phi_0 = \pm\pi$.

D. Boundary TQPT and DPME Jump

In this section, we will show that the slab configuration of the TB model has a boundary gap closing at $\phi_0 = \pm\pi$, which gives a boundary TQPT that changes the relative surface $\mathbb{Z}_2$ index and induces a discontinuous change of the DPME. The TB results are further explained within the low-energy effective theory.

In the TB model, ϕ_0 only appears in the TB model as $\cos(\phi_0)$ and $\sin(\phi_0)$, and thus any TB result must be periodic in ϕ_0. Hence, tuning ϕ_0 from $\pi + 0^-$ to $\pi + 0^+$ should give a jump of the magnetization, as shown in Fig. 3(d). The dramatic difference between the current distributions at $\phi_0 = \pm 0.9$ in Fig. 3(a) provides evidence of the expected jump in the bulk magnetization. Fig. 4(a) suggests that the jump of the DPME at $\phi_0 = \pm\pi$ happens along with the boundary gap closing while the bulk remains gapped. Moreover, the gap closing manifests as one 2D gapless Dirac cone in each valley on each surface perpendicular to x, as shown in Fig. 4(b-d). Because there are two TR-related Dirac cones on one surface at

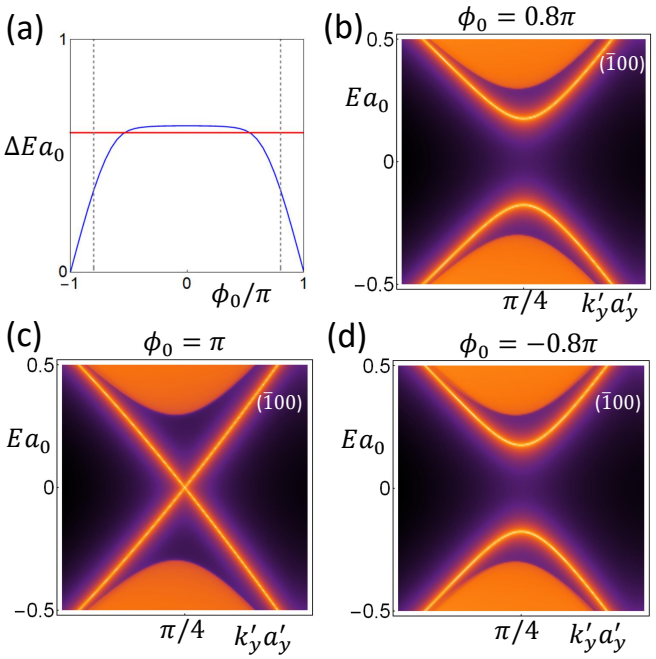

FIG. 4. **Slab and surface calculation of the boundary TQPT in a TR-invariant Weyl-CDW.** (a) The gap of the slab TB model at $(k'_y a'_y, k'_z a'_z) = (\pi/4, 0)$ as a function of ϕ_0 for periodic boundary conditions (red) and open boundary conditions (blue) along only x (keeping the y and z directions periodic). In the simplified TB model used for these calculations, the boundary gap closes at $\phi_0 = \pm\pi$ simultaneously on the top and bottom surfaces. In more realistic TB calculations – examples of which are provided in Appendix C and G5 of the SM – the gap closing on each surface occurs at a different value of ϕ_0. In (b), (c), and (d), we plot the surface spectral function of the $(\bar{1}00)$ surface of the TB model at $\phi_0 = 0.8\pi$, $\phi_0 = \pi$, and $\phi_0 = -0.8\pi$, respectively. In (b), (c), and (d), the dispersion is plotted along $k'_z = 0$ near $k'_y a'_y = \pi/4$.

the gap closing, the surface gap closing has the same form as the 2D $\mathbb{Z}_2$ transition that happens at a TR-related pair of generic momenta[64,69,70]. Because the bulk remains gapped across the transition, the surface gap closings represent examples of boundary TQPTs, which can be detected by jumps in the DPME.

We now interpret the boundary TQPT in the TB model from the perspective of the low-energy theory. According to Eq. (4), one bulk Dirac cone has two mass terms, and thus the bulk gap closing for Eq. (4) requires fine-tuning at least two parameters, which typically does not occur in a realistic model or material. On the $(\bar{1}00)$ surface, the projections of the valleys are along the $m_y\mathcal{T}$-invariant line, and the gap closing along this line only requires fine-tuning one parameter, according to Ref. [21]. The analysis in Ref. [21] further suggests that the gap closing appears as one gapless surface Dirac cone for each valley (Fig. 5(a)) and is thus a surface $\mathbb{Z}_2$ transition, coinciding with the TB results in Fig. 4. The parameter values for which the gap closings appear depend on the boundary condition that we choose in Eq. (4) (see Appendix A and F of the SM for a special boundary condition that realizes both surface gap closings at $\phi_0 = \pi$). Nevertheless, the codimension-1 nature of the gap closing indicates that, even if the boundary conditions are varied, it is still difficult to remove the gap closing point. When the boundary conditions are changed, the gap closing instead shifts to a different value of ϕ_0. This agrees with the picture presented in Ref. [71], in which tuning ϕ_0 pumps 2D TI layers in the WTI phase until a layer reaches the system boundary, causing a surface gap closing. The same argument can also be applied to the (100) surface.

The surface gap closing changes the surface valley Hall conductance by $\pm e^2/2\pi$, which, according to the bulk-boundary correspondence of the axion term, results in a change of the θ_a^{bulk} — or equivalently ϕ_0 — by 2π. Combined with Eq. (18), the 2π jump of ϕ_0 further results in a jump of the magnetization

$$\Delta \boldsymbol{M}_{bulk} = \frac{e\xi_y}{\pi v_y}\mathrm{sgn}(v_x v_y v_z)\dot{u}_{zz}\boldsymbol{e}_y = -\frac{1}{2\pi\sqrt{2}}M_0\boldsymbol{e}_y \ , \tag{22}$$

in which the Fermi velocities have been restored (see Appendix A and F of the SM), and where parameter values shown in the Methods section have been substituted into the second equality. The predicted $\Delta\boldsymbol{M}_{bulk}$ precisely matches the jump given by the TB model in Fig. 3(d). Therefore, the boundary TQPT and the induced jump of the DPME can be captured within the low-energy theory in the limit in which Weyl-point valleys are well-defined.

The above analysis of the discontinuous change of the DPME relies on the fact that the gap closings occur simultaneously on both surfaces of a slab geometry. However, it is important to note that there is no symmetry requirement that the gap closings on opposing surfaces occur simultaneously – with only TR symmetry, the simultaneous surface gap closings represent a fine-tuned limit. Nevertheless, as demonstrated in Appendix B and G of the SM, even if we add an extra term to the TB model to split the accidental simultaneous surface gap closing, a jump in the DPME still occurs across each surface gap closing. Notably though, when the surface gap closures do not occur simultaneously in ϕ_0, the low-energy theory in this case is incapable of fully describing the DPME jump, due to the unavoidable presence of a gapless boundary helical mode on one side of the jump.

III. CONCLUSION AND DISCUSSION

Using low-energy theory and TB calculations, we have in this work introduced the DPME of TR-invariant WSMs in the presence of a bulk-constant (static and homogeneous in the bulk) CDW that gaps the bulk Weyl points. The DPME is a fundamentally 3D strain effect that specifically originates from a valley axion field. We further demonstrate a discontinuous change of the

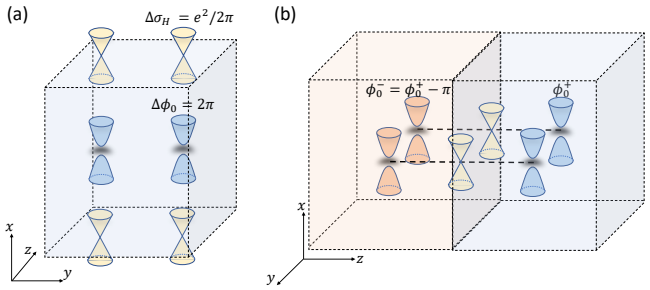

FIG. 5. **Low-energy effective description of the boundary TQPT in a TR-invariant Weyl-CDW.** (a) Gap closings on the surfaces perpendicular to x in a pair of boundary TQPTs. In this figure, we focus on the (artificial) case in which the system is fine-tuned such that gap closings simultaneously occur on both surfaces of a slab geometry. However, as shown in Appendix C and G5 of the SM, the conclusions of this work remain valid away from the fine-tuned limit of simultaneous surface gap closures. (b) 2D gapless Dirac cones at the interface of the domain when the two sides of the domain wall differ by π in ϕ_0. In general, the number of 2D gapless Dirac cones at the interface is $2 + 4n$ where n is a non-negative integer.

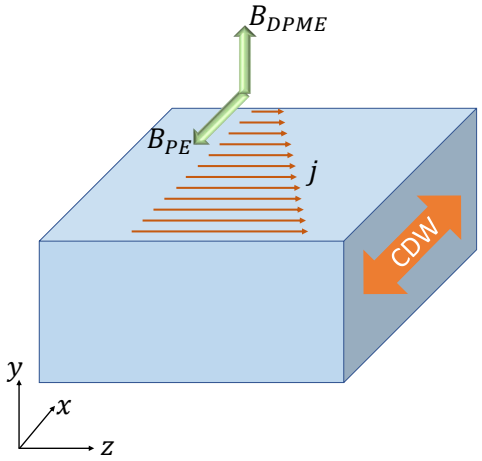

FIG. 6. **A schematic geometry for experimentally probing the DPME.** A sample with finite size along three directions. Outside of the (010) surface, the uniform piezoelectric current generates a magnetic field B_{PE} along x, while the magnetic field B_{DPME} given by the DPME is directed along y. The CDW wavevector is oriented along the x direction.

DPME across a boundary $\mathbb{Z}_2$ TQPT by tuning the phase of the CDW order parameter. The discontinuous change of the DPME can serve as a bulk experimental signature of the boundary TQPT. Although we have only considered a pair of TR-related valleys, the analysis performed in this work can straightforwardly be generalized to multiple pairs of TR-related Weyl points, as long as one does not enforce additional crystalline symmetries that restrict the total DPME to be zero.

To probe the DPME, one can measure the induced magnetic field outside of a Weyl-CDW sample. However, the uniform piezoelectric current also generates a magnetic field outside of the sample, and thus it is important to devise a means of distinguishing the uniform piece from the DPME. One solution is to measure the magnetic field just outside of the (010) surface of a sample with a (100)-directed CDW that gaps the bulk Weyl points. As shown in Fig. 6, the magnetic field given by the DPME in this geometry is directed along y, whereas the magnetic field induced by the uniform piezoelectric current is directed along x. Based on Eq. (21), we estimate the order of magnitude of the response coefficient for the DPME to be $|\partial \boldsymbol{M}/\partial \dot{u}_{zz}| \sim 0.8e/\text{Å}$ for $\xi_y \sim 1eV$[20], $\phi_0 \sim \pi$, and $v_y \sim 10^{-4}c$[72]. We find that the DPME response coefficient has the same units as the 2D piezoelectric coefficient, and thus we may directly compare the value of the DPME response coefficient with typical experimental values of 2D piezoelectric coefficients ($\sim 10^{-20} C/\text{Å}$)[73], suggesting that the above estimated value of the DPME response coefficient is experimentally observable.

In general, it is possible for the system to be in a WTI phase with helical modes on the surfaces perpendicular to y and z, which might influence the observation of the DPME (see Appendix B and G of the SM for further details). Nevertheless, the helical modes can be gapped out by finite-size effects (similar to the gapped side surfaces of the axion insulators[47] and antiferromagnetic topological insulators[37,38]) when the phase of the CDW order parameter and the number of layers are chosen to guarantee that the 2D $\mathbb{Z}_2$ index of the slab is trivial. The helical modes can alternatively be removed by a side-surface CDW[74]. An important direction of future study is to formulate the contribution from the boundary helical mode to the DPME, which is relevant in the case in which there is one gapless helical mode left on the side-surface for certain values of the phase of the CDW order parameter with respect to the number of layers.

In addition to a direct probe of the DPME, the existence of a boundary TQPT predicted by our theory indicates the appearance of 1D gapless helical modes along surface domain walls of the CDW phase (see Appendix. C of the SM for details). The gapless helical domain-wall fermions can in principle be probed through scanning tunneling microscopy. Moreover, it is intriguing to ask whether the boundary TQPT separates two 3D phases with different boundary-obstructed topology[75], and to elucidate the precise relationship between the boundary TQPT and symmetry-enhanced topological surface anomalies[74,76,77].

In this work, we have focused on TR-invariant gapped Weyl-CDWs. TR-invariant WSMs have been realized in a number of non-centrosymmetric systems, including NbAs[78], TaAs[79–82], and $(TaSe_4)_2I$[72,83], and an axionic Weyl-CDW phase has recently been demonstrated in $(TaSe_4)_2I$[51]. We emphasize that the intuitive picture of the DPME is applicable as long as the low-energy physics

of a given system is well-captured by 3D Dirac fermions with complex mass terms. This implies that the DPME may also exist in other 3D Dirac materials[84]. In the current work, we have treated the axion field (or the CDW phase) as a fixed background field. After taking into account the dynamics of CDW (such as a phason), the effective action in Eq. (10) suggests a nonzero coupling between the phason of the CDW and the strain field, implying the intriguing possibility of strain engineering the CDW phase angle in TR-invariant WSMs.

IV. METHODS

A. Low-Energy Action

In this section, we provide further details of the derivation of Eq. (4). The complete discussion of the low-energy effective action is in Appendix A and F of the SM.

A WSM phase can only emerge in systems that either break TR symmetry (magnetic materials) or break inversion symmetry (non-centrosymmetric crystals). CDWs in magnetic WSMs have been previously studied in numerous works, including Ref. [49,50]. In this work, we focus on CDWs in TR-invariant WSMs, which can be realized in non-centrosymmetric crystals. Since two Weyl points related by TR symmetry share the same chirality, and because the total chirality of the whole system must vanish[85], there must be four Weyl points in a minimal model of a TR-invariant WSM. The four Weyl points shown in Eq. (2) are related by TR and mirror symmetries. TR symmetry, labeled as $\mathcal{T}$, relates $\boldsymbol{k}_{1,\alpha}$ to $\boldsymbol{k}_{2,\alpha}$ with the same chirality index α, while the mirror m_y changes the chirality of Weyl points and relates $\boldsymbol{k}_{1,\alpha}$ to $\boldsymbol{k}_{2,-\alpha}$. In the derivation of Eq. (3), we follow Ref. [49,86] and keep $\boldsymbol{k}=0$ as the momentum-space origin of all fermion fields, as this choice naturally includes the Weyl-point-induced valley Hall effect in the effective action.

As mentioned above, both $\mathcal{T}$ and m_y change the valley index a of the fields in Eq. (3), while m_y ($\mathcal{T}$) changes (preserves) the chirality index α. Thus, we can always choose the bases to represent $\mathcal{T}$ and m_y as $\mathrm{i}\sigma_y\mathcal{K}$ and $-\mathrm{i}\sigma_y$ for the band index, respectively, where $\mathcal{K}$ is complex conjugation. According to the above symmetry representation for $\mathcal{T}$ and m_y, a symmetry-preserving mean-field CDW term that couples two Weyl points of the same valley index a can be written as[49]

$$\mathcal{L}_{CDW} = -\sum_a m_a(\boldsymbol{r}) e^{\mathrm{i}(-1)^{a-1}\boldsymbol{Q}\cdot\boldsymbol{r}} \psi^\dagger_{a,+}\psi_{a,-} + h.c. \ , \quad (23)$$

where the $t,\boldsymbol{r}$ dependence of ψ is implied. Throughout this work, we include the spatial dependence of the CDW order parameter $m_a(\boldsymbol{r})$, while keeping the order parameter time-independent (*i.e.* static). TR symmetry requires that $m_1(\boldsymbol{r}) = m_2(\boldsymbol{r})^* \equiv m(\boldsymbol{r})$, and m_y symmetry requires that $m_1^*(m_y\boldsymbol{r}) = m_2(\boldsymbol{r})$. In general, $m(\boldsymbol{r}) = |m(\boldsymbol{r})|e^{\mathrm{i}\phi(\boldsymbol{r})}$ is complex, and $|m(\boldsymbol{r})|$ and $\phi(\boldsymbol{r})$ are the magnitude and phase of the CDW order parameter, respectively. The underlying interaction that gives rise to the bulk CDW is discussed in Appendix D of the SM at the mean-field level. We next introduce the γ matrices

$$\gamma^\mu = (\tau_x\sigma_0, -\mathrm{i}\tau_y\boldsymbol{\sigma})_\mu \ , \ \gamma^5 = \mathrm{i}\gamma^0\gamma^1\gamma^2\gamma^3 \ , \quad (24)$$

where $\mu = 0,1,2,3$ and $\tau_{0,x,y,z}$ are Pauli matrices for the chirality index α. Using the above definitions of the γ matrices, we can rewrite the CDW term as

$$\mathcal{L}_{CDW} = -\sum_a |m(\boldsymbol{r})|\overline{\psi}_a e^{-\mathrm{i}\Phi_a(\boldsymbol{r})\gamma^5}\psi_a \ . \quad (25)$$

The spatial dependence of $|m|, \phi, \Phi_a$ are implicit in the main text unless specified otherwise.

In order to elucidate the strain-induced linear response, we introduce an electron-strain coupling for normal strain (*i.e.* stretch or compression along a specified axis) along the z direction, labeled as $u_{zz}(t)$. We require that the strain be adiabatic, homogeneous, and infinitesimal. Enforcing TR and mirror symmetries, the most general form of the leading-order electron-strain coupling reads

$$\begin{aligned}\mathcal{L}_{str} = \sum_a \overline{\psi}_a[-\xi_0\gamma^0 + (-1)^a(\gamma^1\gamma^5\xi_x + \gamma^2\xi_y \\ + \gamma^3\gamma^5\xi_z)]\psi_a u_{zz} \ ,\end{aligned} \quad (26)$$

where the time dependence of u_{zz} is implied, and where the parameters $\xi_{0,x,y,z}$ are material-dependent. In Eq. (26), we do not include the effects of strain that couple different Weyl points, as Weyl-point coupling strain is necessarily proportional to $|m_0|u_{zz}$, and because $|m_0|$ is typically small in real materials. The detailed procedure of adding the electron-strain coupling is shown in Appendix E of the SM. We set the strain to be uniform throughout all of space, such that the gapped and symmetry-preserving boundary is implemented by the spatial dependence of the CDW order parameter m, as opposed to an inhomogeneous strain field.

Summing up Eq. (3), Eq. (25), and Eq. (26) and including the $U(1)$ gauge field coupling for the electromagnetic field, we arrive at the total low-energy Lagrangian Eq. (4).

B. TB Model

In this section, we provide further details of the TB model used in this work to demonstrate the DPME. Further details of our TB calculations are provided in Appendix B and G of the SM.

We begin by considering an orthorhombic crystal with a sublattice described by a four-component basis $c^\dagger_{\boldsymbol{k},i,s}$, in which $i=1,2$ is the sublattice index and $s=\pm$ is the spin index. using nearest-neighbor hopping terms specified in Appendix B and G of the SM, we choose the following symmetry-allowed form for the strained TB model (without CDW):

$$H_{TB,u} = \sum_{\boldsymbol{k}} c^\dagger_{\boldsymbol{k}} h_{TB,u}(\boldsymbol{k}) c_{\boldsymbol{k}} \ , \quad (27)$$

$$h_{TB,u}(\boldsymbol{k}) = \frac{1}{a_0}\left[d_1\tau_z\sigma_0 + d_2\tau_y\sigma_0 + d_3\tau_x\sigma_x + d_4\tau_x\sigma_z + d_5\tau_y\sigma_x\right] \ , \tag{28}$$

where the $\boldsymbol{k}$ dependence of d's is implied, the strain-induced redefinition of $c_{\boldsymbol{k}}$ discussed in Appendix E of the SM is implied, and where

$$\begin{aligned}
d_1 &= n_0 - 1 + \cos(k_x a_0) + n_2\cos(k_y a_0) + (1-u_{zz})\cos(k_z a_0) \\
d_2 &= (1-\frac{u_{zz}}{5})\sin(k_y a_0)\cos(k_z a_0/2) \\
d_3 &= (1-u_{zz})\sin(k_z a_0/2) \\
d_4 &= (1-\frac{u_{zz}}{5})\cos(k_x a_0)\sin(k_z a_0/2) \\
d_5 &= (1-\frac{u_{zz}}{5})n_1\cos(k_z a_0/2)\cos(k_y a_0) + (1-\frac{u_{zz}}{5})n_3\cos(k_z a_0/2)\cos(k_x a_0) \ .
\end{aligned} \tag{29}$$

Throughout this work, we have taken the inverse of the lattice constant without strain $1/a_0$ as the unit of energy. For concreteness, we then choose

$$n_0 = -\sqrt{2},\ n_1 = 1,\ n_2 = 2,\ n_3 = -1 \ . \tag{30}$$

We next add a CDW term that preserves TR and m_y symmetries into the TB model, where the CDW coupling takes the form

$$\begin{aligned}
H_{TB,CDW} = \sum_{\boldsymbol{k}} c^\dagger_{\boldsymbol{k}+(\frac{\pi}{a_0},0,0)}\left[-\mathrm{i}\mu_1\sin(k_x a_0)M_1(k_y,k_z)\right. \\
\left.+\mu_2 M_2(k_y,k_z)\right]c_{\boldsymbol{k}} \ ,
\end{aligned} \tag{31}$$

where μ_1 and μ_2 are real scalar parameters,

$$M_1 = \left[-\cos(k_z a_0/2)\tau_y\sigma_0 + \tau_z\sigma_x\right]\sin(k_y a_0) \ , \tag{32}$$

and

$$M_2 = \left[-\cos(k_z a_0/2)\tau_y\sigma_x + \tau_z\sigma_0\right]/\sqrt{2} \ . \tag{33}$$

Eq. (31) suggests that the CDW term contains two channels that are characterized by two real coupling constants, μ_1 and μ_2. Throughout this work, we set $|\mu_1 + \mathrm{i}\mu_2| = 0.3/a_0$ for all of the numerical calculations for the TB model in the presence of the CDW.

By projecting to the low-energy modes, the total TB model $H_{TB,u} + H_{TB,CDW}$ reproduces Eq. (3), Eq. (25) and Eq. (26) with

$$v_x = \sqrt{2}\ ,\ v_y = -2\ ,\ v_z = \frac{1}{2}\ , \tag{34}$$

$$m_0 = (\mu_1 + \mathrm{i}\mu_2)e^{-\mathrm{i}2\varphi} \Rightarrow \phi_0 = \arg(\mu_1 + \mathrm{i}\mu_2) - 2\varphi \ , \tag{35}$$

and

$$\xi_0 = \xi_z = 0\ ,\ \xi_x = \frac{1}{\sqrt{2}a_0}\ ,\ \xi_y = -\frac{1}{\sqrt{2}a_0}\ , \tag{36}$$

where φ is the $U(1)$ gauge degree of freedom of the eigenvectors (further discussed in Appendix B and G of the SM). Throughout this work, we have chosen $\phi_0 = \arg(\mu_1 + \mathrm{i}\mu_2)$ by setting $\varphi = 0$ unless otherwise specified.

V. ACKNOWLEDGEMENTS

J.Y. and C.X.L thank Wladimir A. Benalcazar and Radu Roiban, B.J.W. thanks Barry Bradlyn, and all authors thank B. Andrei Bernevig for helpful discussions. The work done at Penn State, including all analytical derivation and numerical calculation, is primarily supported by the DOE grant (DE-SC0019064). B.J.W. acknowledges support from B. Andrei Bernevig through Department of Energy Grant No. DESC0016239, Simons Investigator Grant No. 404513, BSF Israel US Foundation Grant No. 2018226, ONR Grant No. N00014-20-1-2303, and the Gordon and Betty Moore Foundation through Grant No. GBMF8685 towards the Princeton theory program.

During the final stages of preparing this work, an updated version of Ref. [71] demonstrated that TR-invariant Dirac-CDWs are topologically equivalent to ϕ_0-dependent WTIs. The results of Ref. [71] are complementary to and in complete agreement with the results of this work.

* cxl56@psu.edu

[1] M. Z. Hasan and C. L. Kane, "Colloquium: Topological

insulators," Rev. Mod. Phys. **82**, 3045–3067 (2010).

[2] Xiao-Liang Qi and Shou-Cheng Zhang, "Topological insulators and superconductors," Rev. Mod. Phys. **83**, 1057–1110 (2011).

[3] K. v. Klitzing, G. Dorda, and M. Pepper, "New method for high-accuracy determination of the fine-structure constant based on quantized hall resistance," Phys. Rev. Lett. **45**, 494–497 (1980).

[4] D. J. Thouless, M. Kohmoto, M. P. Nightingale, and M. den Nijs, "Quantized hall conductance in a two-dimensional periodic potential," Phys. Rev. Lett. **49**, 405–408 (1982).

[5] F. D. M. Haldane, "Model for a quantum hall effect without landau levels: Condensed-matter realization of the "parity anomaly"," Phys. Rev. Lett. **61**, 2015–2018 (1988).

[6] Cui-Zu Chang, Jinsong Zhang, Xiao Feng, Jie Shen, Zuocheng Zhang, Minghua Guo, Kang Li, Yunbo Ou, Pang Wei, Li-Li Wang, Zhong-Qing Ji, Yang Feng, Shuaihua Ji, Xi Chen, Jinfeng Jia, Xi Dai, Zhong Fang, Shou-Cheng Zhang, Ke He, Yayu Wang, Li Lu, Xu-Cun Ma, and Qi-Kun Xue, "Experimental observation of the quantum anomalous hall effect in a magnetic topological insulator," Science **340**, 167–170 (2013).

[7] Naoto Nagaosa, Jairo Sinova, Shigeki Onoda, A. H. MacDonald, and N. P. Ong, "Anomalous hall effect," Rev. Mod. Phys. **82**, 1539–1592 (2010).

[8] Di Xiao, Junren Shi, and Qian Niu, "Berry phase correction to electron density of states in solids," Phys. Rev. Lett. **95**, 137204 (2005).

[9] Di Xiao, Yugui Yao, Zhong Fang, and Qian Niu, "Berry-phase effect in anomalous thermoelectric transport," Phys. Rev. Lett. **97**, 026603 (2006).

[10] Di Xiao, Ming-Che Chang, and Qian Niu, "Berry phase effects on electronic properties," Rev. Mod. Phys. **82**, 1959–2007 (2010).

[11] Inti Sodemann and Liang Fu, "Quantum nonlinear hall effect induced by berry curvature dipole in time-reversal invariant materials," Phys. Rev. Lett. **115**, 216806 (2015).

[12] Yang Zhang, Yan Sun, and Binghai Yan, "Berry curvature dipole in weyl semimetal materials: An ab initio study," Phys. Rev. B **97**, 041101 (2018).

[13] Su-Yang Xu, Qiong Ma, Huitao Shen, Valla Fatemi, Sanfeng Wu, Tay-Rong Chang, Guoqing Chang, Andrés M. Mier Valdivia, Ching-Kit Chan, Quinn D. Gibson, Jiadong Zhou, Zheng Liu, Kenji Watanabe, Takashi Taniguchi, Hsin Lin, Robert J. Cava, Liang Fu, Nuh Gedik, and Pablo Jarillo-Herrero, "Electrically switchable berry curvature dipole in the monolayer topological insulator wte2," Nature Physics **14**, 900–906 (2018).

[14] Qiong Ma, Su-Yang Xu, Huitao Shen, David MacNeill, Valla Fatemi, Tay-Rong Chang, Andres M Mier Valdivia, Sanfeng Wu, Zongzheng Du, Chuang-Han Hsu, *et al.*, "Observation of the nonlinear hall effect under time-reversal-symmetric conditions," Nature **565**, 337–342 (2019).

[15] Kaifei Kang, Tingxin Li, Egon Sohn, Jie Shan, and Kin Fai Mak, "Nonlinear anomalous hall effect in few-layer wte2," Nature Materials **18**, 324–328 (2019).

[16] Richard M. Martin, "Piezoelectricity," Phys. Rev. B **5**, 1607–1613 (1972).

[17] D Vanderbilt, "Berry-phase theory of proper piezoelectric response," Journal of Physics and Chemistry of Solids **61**, 147 – 151 (2000).

[18] Abolhassan Vaezi, Nima Abedpour, Reza Asgari, Alberto Cortijo, and María A. H. Vozmediano, "Topological electric current from time-dependent elastic deformations in graphene," Phys. Rev. B **88**, 125406 (2013).

[19] Matthias Droth, Guido Burkard, and Vitor M. Pereira, "Piezoelectricity in planar boron nitride via a geometric phase," Phys. Rev. B **94**, 075404 (2016).

[20] Habib Rostami, Francisco Guinea, Marco Polini, and Rafael Roldán, "Piezoelectricity and valley chern number in inhomogeneous hexagonal 2d crystals," npj 2D Materials and Applications **2**, 15 (2018).

[21] Jiabin Yu and Chao-Xing Liu, "Piezoelectricity and topological quantum phase transitions in two-dimensional spin-orbit coupled crystals with time-reversal symmetry," Nature Communications **11**, 2290 (2020).

[22] Xiao-Liang Qi, Taylor L. Hughes, and Shou-Cheng Zhang, "Topological field theory of time-reversal invariant insulators," Phys. Rev. B **78**, 195424 (2008).

[23] Andrew M. Essin, Joel E. Moore, and David Vanderbilt, "Magnetoelectric polarizability and axion electrodynamics in crystalline insulators," Phys. Rev. Lett. **102**, 146805 (2009).

[24] Zhong Wang, Xiao-Liang Qi, and Shou-Cheng Zhang, "Equivalent topological invariants of topological insulators," New Journal of Physics **12**, 065007 (2010).

[25] Taylor L. Hughes, Emil Prodan, and B. Andrei Bernevig, "Inversion-symmetric topological insulators," Phys. Rev. B **83**, 245132 (2011).

[26] Ari M. Turner, Yi Zhang, Roger S. K. Mong, and Ashvin Vishwanath, "Quantized response and topology of magnetic insulators with inversion symmetry," Phys. Rev. B **85**, 165120 (2012).

[27] Chen Fang, Matthew J. Gilbert, and B. Andrei Bernevig, "Bulk topological invariants in noninteracting point group symmetric insulators," Phys. Rev. B **86**, 115112 (2012).

[28] Dániel Varjas, Fernando de Juan, and Yuan-Ming Lu, "Bulk invariants and topological response in insulators and superconductors with nonsymmorphic symmetries," Phys. Rev. B **92**, 195116 (2015).

[29] Nicodemos Varnava and David Vanderbilt, "Surfaces of axion insulators," Phys. Rev. B **98**, 245117 (2018).

[30] Frank Schindler, Ashley M. Cook, Maia G. Vergniory, Zhijun Wang, Stuart S. P. Parkin, B. Andrei Bernevig, and Titus Neupert, "Higher-order topological insulators," Science Advances **4** (2018), 10.1126/sciadv.aat0346.

[31] Benjamin J Wieder and B Andrei Bernevig, "The axion insulator as a pump of fragile topology," arXiv:1810.02373 (2018).

[32] Yuanfeng Xu, Zhida Song, Zhijun Wang, Hongming Weng, and Xi Dai, "Higher-order topology of the axion insulator euin$_2$as$_2$," Phys. Rev. Lett. **122**, 256402 (2019).

[33] Junyeong Ahn and Bohm-Jung Yang, "Symmetry representation approach to topological invariants in $C_{2z}t$-symmetric systems," Phys. Rev. B **99**, 235125 (2019).

[34] Nicodemos Varnava, Ivo Souza, and David Vanderbilt, "Axion coupling in the hybrid wannier representation," Phys. Rev. B **101**, 155130 (2020).

[35] Heqiu Li and Kai Sun, "Pfaffian formalism for higher-order topological insulators," Phys. Rev. Lett. **124**, 036401 (2020).

[36] Jiabin Yu, Zhi-Da Song, and Chao-Xing Liu, "Gapless criterion for crystals from effective axion field," Phys. Rev. Lett. **125**, 036401 (2020).

[37] Dongqin Zhang, Minji Shi, Tongshuai Zhu, Dingyu Xing, Haijun Zhang, and Jing Wang, "Topological axion states in the magnetic insulator mnbi$_2$te$_4$ with the quan-

tized magnetoelectric effect," Phys. Rev. Lett. **122**, 206401 (2019).
[38] Na Hyun Jo, Lin-Lin Wang, Robert-Jan Slager, Jiaqiang Yan, Yun Wu, Kyungchan Lee, Benjamin Schrunk, Ashvin Vishwanath, and Adam Kaminski, "Intrinsic axion insulating behavior in antiferromagnetic $mnbi_6te_{10}$," Phys. Rev. B **102**, 045130 (2020).
[39] Jiabin Yu, Jiadong Zang, and Chao-Xing Liu, "Magnetic resonance induced pseudoelectric field and giant current response in axion insulators," Phys. Rev. B **100**, 075303 (2019).
[40] Zhaochen Liu and Jing Wang, "Anisotropic topological magnetoelectric effect in axion insulators," Phys. Rev. B **101**, 205130 (2020).
[41] Zhaochen Liu, Jiang Xiao, and Jing Wang, "Dynamical magnetoelectric coupling in axion insulator thin films," arXiv:2007.09869 (2020).
[42] Liang Wu, M Salehi, N Koirala, J Moon, S Oh, and N-P Armitage, "Quantized faraday and kerr rotation and axion electrodynamics of a 3d topological insulator," Science **354**, 1124–1127 (2016).
[43] Ken N Okada, Youtarou Takahashi, Masataka Mogi, Ryutaro Yoshimi, Atsushi Tsukazaki, Kei S Takahashi, Naoki Ogawa, Masashi Kawasaki, and Yoshinori Tokura, "Terahertz spectroscopy on faraday and kerr rotations in a quantum anomalous hall state," Nature communications **7**, 12245 (2016).
[44] V Dziom, A Shuvaev, A Pimenov, GV Astakhov, C Ames, K Bendias, J Böttcher, G Tkachov, EM Hankiewicz, C Brüne, *et al.*, "Observation of the universal magnetoelectric effect in a 3d topological insulator," Nature communications **8**, 15197 (2017).
[45] Jing Wang, Biao Lian, Xiao-Liang Qi, and Shou-Cheng Zhang, "Quantized topological magnetoelectric effect of the zero-plateau quantum anomalous hall state," Phys. Rev. B **92**, 081107 (2015).
[46] Masataka Mogi, Minoru Kawamura, Atsushi Tsukazaki, Ryutaro Yoshimi, Kei S. Takahashi, Masashi Kawasaki, and Yoshinori Tokura, "Tailoring tricolor structure of magnetic topological insulator for robust axion insulator," Science Advances **3** (2017), 10.1126/sciadv.aao1669.
[47] Di Xiao, Jue Jiang, Jae-Ho Shin, Wenbo Wang, Fei Wang, Yi-Fan Zhao, Chaoxing Liu, Weida Wu, Moses H. W. Chan, Nitin Samarth, and Cui-Zu Chang, "Realization of the axion insulator state in quantum anomalous hall sandwich heterostructures," Phys. Rev. Lett. **120**, 056801 (2018).
[48] Xiao-Liang Qi, Rundong Li, Jiadong Zang, and Shou-Cheng Zhang, "Inducing a magnetic monopole with topological surface states," Science **323**, 1184–1187 (2009).
[49] Zhong Wang and Shou-Cheng Zhang, "Chiral anomaly, charge density waves, and axion strings from weyl semimetals," Phys. Rev. B **87**, 161107 (2013).
[50] Bitan Roy and Jay D. Sau, "Magnetic catalysis and axionic charge density wave in weyl semimetals," Phys. Rev. B **92**, 125141 (2015).
[51] J. Gooth, B. Bradlyn, S. Honnali, C. Schindler, N. Kumar, J. Noky, Y. Qi, C. Shekhar, Y. Sun, Z. Wang, B. A. Bernevig, and C. Felser, "Axionic charge-density wave in the weyl semimetal (tase4)2i," Nature **575**, 315–319 (2019).
[52] Alberto Cortijo, Yago Ferreirós, Karl Landsteiner, and María A. H. Vozmediano, "Elastic gauge fields in weyl semimetals," Phys. Rev. Lett. **115**, 177202 (2015).
[53] Alberto Cortijo, Dmitri Kharzeev, Karl Landsteiner, and Maria A. H. Vozmediano, "Strain-induced chiral magnetic effect in weyl semimetals," Phys. Rev. B **94**, 241405 (2016).
[54] D. I. Pikulin, Anffany Chen, and M. Franz, "Chiral anomaly from strain-induced gauge fields in dirac and weyl semimetals," Phys. Rev. X **6**, 041021 (2016).
[55] Yizhi You, Gil Young Cho, and Taylor L. Hughes, "Response properties of axion insulators and weyl semimetals driven by screw dislocations and dynamical axion strings," Phys. Rev. B **94**, 085102 (2016).
[56] Sthitadhi Roy, Michael Kolodrubetz, Nathan Goldman, and Adolfo G Grushin, "Tunable axial gauge fields in engineered weyl semimetals: semiclassical analysis and optical lattice implementations," 2D Materials **5**, 024001 (2018).
[57] Rodrigo Soto-Garrido and Enrique Muñoz, "Electronic transport in torsional strained weyl semimetals," Journal of Physics: Condensed Matter **30**, 195302 (2018).
[58] Valerio Peri, Marc Serra-Garcia, Roni Ilan, and Sebastian D. Huber, "Axial-field-induced chiral channels in an acoustic weyl system," Nature Physics **15**, 357–361 (2019).
[59] Jan Behrends, Roni Ilan, and Jens H. Bardarson, "Anomalous conductance scaling in strained weyl semimetals," Phys. Rev. Research **1**, 032028 (2019).
[60] Enrique Muñoz and Rodrigo Soto-Garrido, "Thermoelectric transport in torsional strained weyl semimetals," Journal of Applied Physics **125**, 082507 (2019).
[61] Shiva Heidari and Reza Asgari, "Chiral hall effect in strained weyl semimetals," Phys. Rev. B **101**, 165309 (2020).
[62] Roni Ilan, Adolfo G. Grushin, and Dmitry I. Pikulin, "Pseudo-electromagnetic fields in 3d topological semimetals," Nature Reviews Physics **2**, 29–41 (2020).
[63] P. O. Sukhachov and H. Rostami, "Acoustogalvanic effect in dirac and weyl semimetals," Phys. Rev. Lett. **124**, 126602 (2020).
[64] C. L. Kane and E. J. Mele, "Z_2 topological order and the quantum spin hall effect," Phys. Rev. Lett. **95**, 146802 (2005).
[65] IE Dzialoshinskii, "The problem of piezomagnetism," Sov. Phys. JETP **6**, 621–622 (1958).
[66] Mark Srednicki, *Quantum field theory* (Cambridge University Press, 2007).
[67] Reinhold A Bertlmann, *Anomalies in quantum field theory*, Vol. 91 (Oxford University Press, 2000).
[68] Dan Sehayek, Manisha Thakurathi, and A. A. Burkov, "Charge density waves in weyl semimetals," Phys. Rev. B **102**, 115159 (2020).
[69] J. E. Moore and L. Balents, "Topological invariants of time-reversal-invariant band structures," Phys. Rev. B **75**, 121306 (2007).
[70] Shuichi Murakami, Satoshi Iso, Yshai Avishai, Masaru Onoda, and Naoto Nagaosa, "Tuning phase transition between quantum spin hall and ordinary insulating phases," Phys. Rev. B **76**, 205304 (2007).
[71] Benjamin J. Wieder, Kuan-Sen Lin, and Barry Bradlyn, "Axionic band topology in inversion-symmetric weyl-charge-density waves," Phys. Rev. Research **2**, 042010 (2020).
[72] Wujun Shi, Benjamin J. Wieder, Holger L. Meyerheim, Yan Sun, Yang Zhang, Yiwei Li, Lei Shen, Yanpeng Qi, Lexian Yang, Jagannath Jena, Peter Werner, Klaus Koepernik, Stuart Parkin, Yulin Chen, Claudia Felser, B. Andrei Bernevig, and Zhijun Wang, "A charge-density-wave topological semimetal," Nature Physics (2021),

10.1038/s41567-020-01104-z.
[73] Hanyu Zhu, Yuan Wang, Jun Xiao, Ming Liu, Shaomin Xiong, Zi Jing Wong, Ziliang Ye, Yu Ye, Xiaobo Yin, and Xiang Zhang, "Observation of piezoelectricity in free-standing monolayer mos2," Nature Nanotechnology **10**, 151 EP – (2014).
[74] Chao-Xing Liu, Xiao-Liang Qi, and Shou-Cheng Zhang, "Half quantum spin hall effect on the surface of weak topological insulators," Physica E: Low-dimensional Systems and Nanostructures **44**, 906–911 (2012).
[75] Eslam Khalaf, Wladimir A Benalcazar, Taylor L Hughes, and Raquel Queiroz, "Boundary-obstructed topological phases," arXiv:1908.00011 (2019).
[76] Benjamin J. Wieder, Barry Bradlyn, Zhijun Wang, Jennifer Cano, Youngkuk Kim, Hyeong-Seok D. Kim, Andrew M. Rappe, C. L. Kane, and B. Andrei Bernevig, "Wallpaper fermions and the nonsymmorphic dirac insulator," Science **361**, 246–251 (2018).
[77] Chen Fang and Liang Fu, "New classes of topological crystalline insulators having surface rotation anomaly," Science Advances **5** (2019), 10.1126/sciadv.aat2374.
[78] Su-Yang Xu, Nasser Alidoust, Ilya Belopolski, Zhujun Yuan, Guang Bian, Tay-Rong Chang, Hao Zheng, Vladimir N. Strocov, Daniel S. Sanchez, Guoqing Chang, Chenglong Zhang, Daixiang Mou, Yun Wu, Lunan Huang, Chi-Cheng Lee, Shin-Ming Huang, BaoKai Wang, Arun Bansil, Horng-Tay Jeng, Titus Neupert, Adam Kaminski, Hsin Lin, Shuang Jia, and M. Zahid Hasan, "Discovery of a weyl fermion state with fermi arcs in niobium arsenide," Nature Physics **11**, 748–754 (2015).
[79] Su-Yang Xu, Ilya Belopolski, Nasser Alidoust, Madhab Neupane, Guang Bian, Chenglong Zhang, Raman Sankar, Guoqing Chang, Zhujun Yuan, Chi-Cheng Lee, *et al.*, "Discovery of a weyl fermion semimetal and topological fermi arcs," Science **349**, 613–617 (2015).
[80] LX Yang, ZK Liu, Yan Sun, Han Peng, HF Yang, Teng Zhang, Bo Zhou, Yi Zhang, YF Guo, Marein Rahn, *et al.*, "Weyl semimetal phase in the non-centrosymmetric compound taas," Nature physics **11**, 728–732 (2015).
[81] B. Q. Lv, N. Xu, H. M. Weng, J. Z. Ma, P. Richard, X. C. Huang, L. X. Zhao, G. F. Chen, C. E. Matt, F. Bisti, V. N. Strocov, J. Mesot, Z. Fang, X. Dai, T. Qian, M. Shi, and H. Ding, "Observation of weyl nodes in taas," Nature Physics **11**, 724–727 (2015).
[82] B. Q. Lv, H. M. Weng, B. B. Fu, X. P. Wang, H. Miao, J. Ma, P. Richard, X. C. Huang, L. X. Zhao, G. F. Chen, Z. Fang, X. Dai, T. Qian, and H. Ding, "Experimental discovery of weyl semimetal taas," Phys. Rev. X **5**, 031013 (2015).
[83] Xiao-Ping Li, Ke Deng, Botao Fu, YongKai Li, DaShuai Ma, JunFeng Han, Jianhui Zhou, Shuyun Zhou, and Yugui Yao, "Type-iii weyl semimetals and its materialization," arXiv:1909.12178 (2019).
[84] Rui-Xing Zhang, Jimmy A. Hutasoit, Yan Sun, Binghai Yan, Cenke Xu, and Chao-Xing Liu, "Topological nematic phase in dirac semimetals," Phys. Rev. B **93**, 041108 (2016).
[85] H.B. Nielsen and M. Ninomiya, "A no-go theorem for regularizing chiral fermions," Physics Letters B **105**, 219 – 223 (1981).
[86] A. A. Zyuzin and A. A. Burkov, "Topological response in weyl semimetals and the chiral anomaly," Phys. Rev. B **86**, 115133 (2012).

Supplementary Files

This is a list of supplementary files associated with this preprint. Click to download.

- DPMENatCommSM.pdf